Near Surface Geophysics, 2004, 223-230

Imaging scattered seismic surface waves

X. Campman[1,*], K. van Wijk[2], C.D. Riyanti[1], J. Scales[2] and G. Herman[1,3]

[1] *TU Delft, Department of Applied Mathematics, P.O. Box 5031, 2600 GA, Delft, The Netherlands*

[2] *Physical Acoustic Laboratory, Colorado School of Mines, Golden, Colorado 80401, USA*

[3] *Shell International E&P, Rijswijk, The Netherlands*

Received January 2004, revision accepted August 2004

ABSTRACT

Surface-wave analysis is a key tool for seismologists, ranging from near-surface characterization in geotechnical applications to global seismology. Even in exploration seismology, where surface waves are regarded as a kind of noise, the fact that they typically represent the bulk of the recorded energy makes an understanding of surface-wave propagation important. On the other hand, the heterogeneity of the near surface can make such analyses difficult since the heterogeneity is responsible for scattering and mode conversion.

Here, we show how multichannel seismic records of scattered surface waves can be used to obtain spatial images of the heterogeneity. We discuss both data processing and imaging and illustrate our method on laboratory-scale data. Further, synthetic examples show that we can locate individual scatterers accurately, even when many scatterers produce interfering surface waves. Our laboratory results show that the method has the potential to locate near-surface heterogeneities in the field.

INTRODUCTION

Surface waves play a curious role in seismic methods. In geotechnical engineering they provide valuable information about mechanical properties of the shallow subsurface, while in oil exploration they are considered as noise that blurs target reflectors at greater depth.

In near-surface studies, modal analysis of surface waves is used to infer depth-dependent velocity profiles, a method well-established in global seismology (e.g. Nolet 1977). More recently, this technique has also become popular in geotechnical engineering (e.g. Stokoe *et al*. 1994), where it is often referred to as spectral analysis of surface waves (SASW). These methods are based on measurements with either one or two source–receiver pairs. Park *et al*. (1999) proposed multichannel analysis of surface waves, making it possible to resolve higher modes of surface waves better and to separate them from noise, such as energy scattered by source-generated surface waves (ground roll).

Surface waves can also be used for locating and detecting near-surface objects. Park *et al*. (1998), Behoodian *et al*. (1999) and Leparoux *et al*. (2000), for example, processed ground roll in such a way that it is useful for locating underground objects. However, only a few attempts have been made so far actually to image scattered surface waves (Snieder 1987; Blonk *et al*. 1995; Herman *et al*. 2000).

The advent of multichannel surface-wave recording has opened the way for developing alternative processing methods for scattered surface waves. Here, we describe a model for the propagation and scattering of surface waves close to a linear or areal receiver array by introducing a frequency-dependent impedance function that contains the contrast of the heterogeneities, lumped at the surface. Based on this model, we propose a scheme to process surface-wave data into images of near-surface heterogeneities.

To validate this method, we measure the vertical component of (scattered) surface waves on the surface of an aluminum block. The data are collected in a square region over a cavity in the surface of the model, using a computer-controlled, fully non-contacting, ultrasonic acquisition system. The dense sampling of the wavefield at the surface allows maximum insight into the scattering process, greatly contributing to our understanding of near-surface scattering. Using data from this experiment, we accurately locate the cavity and reconstruct its shape. To investigate whether we can also resolve individual scatterers when scattered surface waves interfere, we image synthetic data from near-surface scattering models with multiple scatterers. Our images show the correct location and relative strength of individual scatterers.

METHOD

A general outline of our method is shown in Fig. 1. From the field record, we first select a suitable event (box 1). Usually, this will be the direct-arrival ground roll. Next, we estimate the surface-wave velocity (box 2). In general, the fundamental-mode Rayleigh-wave velocity is satisfactory. This can be estimated from the data, or can even be measured in the field. Processing

* campman@math.tudelft.nl

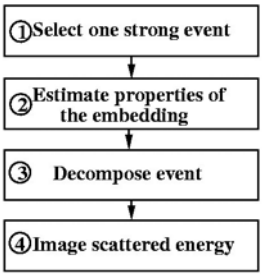

FIGURE 1
Scheme for our method for imaging scattered surface waves

consists of separating the wavefield scattered by near-surface heterogeneities from the selected event (box 3). Although we only discuss surface-wave to surface-wave scattering here, scattered surface waves excited by upcoming body waves when they impinge on near-surface heterogeneities are also contained in our formulation and similar results can be obtained from them. After separating the scattered field, the impedance function (i.e. the image) is determined by inversion (box 4). The image obtained in this way is a spatial distribution of subsurface heterogeneities, proportional to the contrast of the background with the heterogeneity. The information about the depth and, possibly, the vertical size of the heterogeneity in the impedance function obtained, has yet to be investigated.

Near-surface scattering model

We consider scattering of surface waves by heterogeneities close to the surface of a (laterally) homogeneous elastic half-space. Due to the linearity of the elastic wavefield, the vertical component of the particle velocity can be written as

$$v(\mathbf{x},t) = v^{\mathrm{inc}}(\mathbf{x},t) + v^{\mathrm{sc}}(\mathbf{x},t), \tag{1}$$

where v^{inc} is the field that would have been measured if the region under the receivers were homogeneous and v^{sc} is the field due to scattering from heterogeneities immediately under the receivers. In (1), $\mathbf{x} = (x, y, z)$ denotes position and t denotes time. From the elastic-wave equation for particle displacement, we can derive an expression for the scattered field in terms of vertical velocity measured at the surface, due to a vertical point source at $\mathbf{x}^{\mathrm{S}} = (x^{\mathrm{S}}, y^{\mathrm{S}}, 0)$ (Campman *et al*. 2004):

$$v^{\mathrm{sc}}(\mathbf{x}_l,\omega,\mathbf{x}^{\mathrm{S}}) = \int_{\mathbf{x}'_l\in\Sigma} u^{\mathrm{G}}(\mathbf{x}_l-\mathbf{x}'_l,\omega)\sigma(\mathbf{x}'_l,\omega)v(\mathbf{x}'_l,\omega,\mathbf{x}^{\mathrm{S}})\mathrm{d}\mathbf{x}'_l, \tag{2}$$

where the surface $\sum$ is the domain occupied by the receivers and $\mathbf{x}_l = (x, y)$ denotes the horizontal coordinate while ω denotes a regular frequency. Here, u^{G} is the impulse response (or Green's function) of the shallow subsurface and σ is a surface impedance function accounting for the contrasting heterogeneities. The impedance function is defined as

$$\sigma(\mathbf{x}_l,\omega) = \Delta z\omega^2\rho^1(\mathbf{x}_l), \tag{3}$$

where $\rho^1(\mathbf{x}) = \rho(\mathbf{x}) - \rho^0$ is the density contrast between the embedding medium (ρ^0) and the scatterer (ρ). In eq. (2) we assume that scattering takes place close to the surface so that we can replace the field at the scattering depth by the field measured at the receivers. In this way, we collect all scattering into a layer at the surface. The thickness of this layer is denoted by Δz. By allowing the impedance to depend on frequency we account, to a certain extent, for variations in the actual depth of the heterogeneities while this also takes care of dispersion not accounted for in our model. The integral is over a surface, thus we express scattering by volume scatterers in terms of a surface impedance function. This type of model was also used by Blonk *et al*. (1995).

In deriving the Green's function, we assume that the horizontal displacements excited by the vertical source are negligible compared to the vertical displacement. In doing so, the elastic problem is reduced to a scalar problem. Consequently, we neglect interactions between different components of the wavefield. This type of model was proposed to find expressions for vertical stress in soils by Westergaard (1938), and for media with horizontal constraints by Harr (1966). Los *et al*. (2001) showed that this assumption can be applied to propagation of surface waves and is justified for observations close to the (scatter) source.

Imaging

Equation (1) expresses the decomposition of the wavefield measured at the geophones into two parts: one part that propagates in the embedding medium as if there were no scatterers (the incident wavefield) and one part that accounts for the presence of the scatterers (the scattered wavefield). Without making any assumptions about the subsurface, we can thus look for a smooth part and then attribute any rapid variations in the wavefield to the presence of scatterers close to the surface. This will be discussed in a following example. First, we select a suitable event from the field record. It should be a distinct event separated in time from other events. In general, the direct Rayleigh wave is a good candidate. Then, having obtained a good estimate of the scattered field, we write

$$v^{\mathrm{sc}} = K\sigma, \tag{4}$$

where σ is the surface impedance function and the operator K is defined as (equation (2)):

$$\{K\sigma\}(\mathbf{x}_l,\omega) = \int_{\mathbf{x}'_l\in\Sigma} u_z^{\mathrm{G}}(\mathbf{x}_l-\mathbf{x}'_l,\omega)\sigma(\mathbf{x}'_l,\omega)v^{\mathrm{meas}}(\mathbf{x}'_l,\omega)\mathrm{d}\mathbf{x}'_l.$$

Here, we have substituted the field measured at the receivers (v^{meas}) for the field in the integral on the right-hand side of equation (2), leaving σ the only unknown. Finding the impedance function is posed as a minimization problem, i.e. we look for the impedance function (or the image) to minimize the following objective function:

$$F = \frac{\| v^{\mathrm{sc}} - K\sigma \|^2}{\| v^{\mathrm{sc}} \|^2} + \lambda \| \sigma \|^2, \tag{5}$$

where λ is a regularization parameter, determining the weight given to minimization of the norm of the estimated model σ relative to minimization of the residual norm. Without prior knowledge of the data uncertainty, we use the *L*-curve method (Hansen 1997) to choose an optimal value for λ.

Note that our surface-wave imaging method bears much resemblance to the imaging scheme described by Tarantola (1984). However, the main difference is that we image waves travelling along the surface instead of imaging body waves.

LABORATORY EXPERIMENT

Description of the experiment

We measure the vertical component of the particle velocity on the surface of an aluminum block, excited by a pulsed infra-red laser in the thermo-elastic regime (Scales and Malcolm 2003). We focused the laser beam on a 21 mm line, thus simulating a line source. This source generates surface waves that are scattered by a cylindrical cavity with a diameter of 2 mm and a depth of 3 mm, which is roughly the size of the dominant wavelength. The wavefield is detected using a scanning laser interferometer that measures the vertical component of the particle velocity on the surface of the model via the Doppler shift (Nishizawa *et al*. 1997; Scales and van Wijk 1999). Traces are recorded at 0.25 mm intervals, implying about 10 traces per wavelength. Figure 2 illustrates the top view of the experimental configuration, while Fig. 3 is a snapshot of the wavefield passing through the cavity from right to left, clearly showing the scattered surface wave. (A movie of the experiment described in this paper can be downloaded from http://acoustics.mines.edu/research.) The total area covered by 81×81 detectors is 20×20 mm^2. For the examples, we use only a part of the data, indicated by the dashed line in Fig. 2 (41×41 receivers).

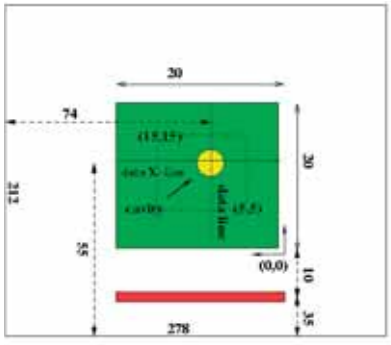

FIGURE 2

Top view of the aluminum block with cavity. The shaded area is the area covered by the receivers. The source width (dark shade) is 0.5 mm. Dimensions in the figure are given in millimetres.

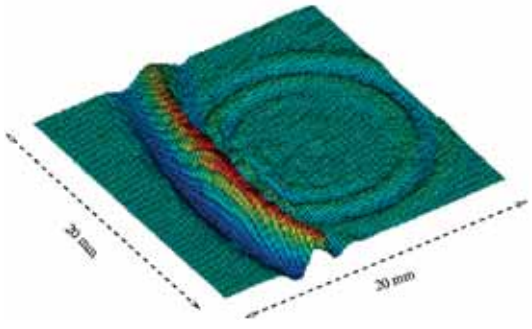

FIGURE 3

Snapshot of the direct Rayleigh wave when it passed through the cavity (from right to left). The scattered Rayleigh wave is clearly visible.

Results for experiment I

Wavefield separation

Figure 4 shows part of the data in the in-line direction above the cavity. The incident Rayleigh wave is strongly perturbed by the cavity as is evident from the scattering visible between about 9.5 and 12.5 mm. Moreover, we observe a scattered Rayleigh wave that is also clearly visible in the snapshot (Fig. 3).

The objective of this method is to obtain accurate images of heterogeneities under the receivers. Due to the decay of Rayleigh waves with depth (e.g. Aki and Richards 1980), and because of the simplifying assumptions made during the course of deriving our scattering model, we expect to get accurate images only for depths up to about half the Rayleigh wavelength (Campman *et al*. 2004). In this case, scatterers are in the near-field and, in general, scattering interferes with the incident wave (as in Fig. 3, for example). For this reason, careful processing to separate the wavefield components is required. Moreover, the incident wave contains propagation effects from the source to the scattering domain close to the receivers and can therefore be complicated. In such cases, wavefield separation techniques like those used in VSP data processing may have to be applied (Mars *et al*. 1999). Once we have isolated the direct Rayleigh wave, together with the scattering 'tail' from the shot record by time windowing, we then separate the scattered energy from this event. Aided by the dense spatial sampling of the wavefield and due to the fact that

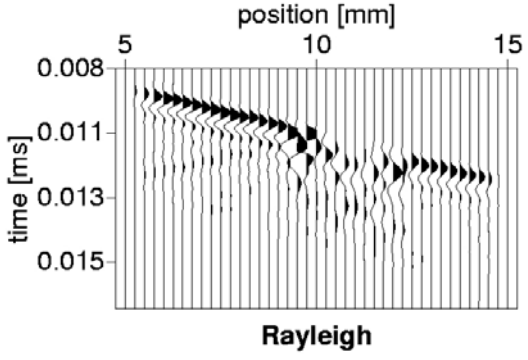

FIGURE 4

Display of the direct Rayleigh wave (R) on a line above the cavity. The Rayleigh wave reflected off the cavity is labelled S.

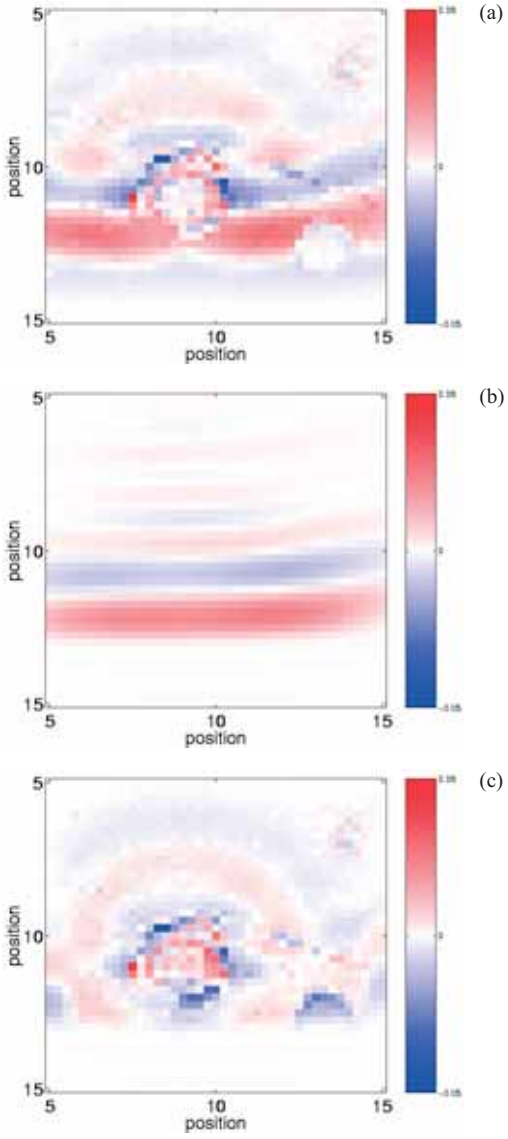

FIGURE 5
(a) Top view of the total field (v). (b) The estimated incident field (v^{inc}) separated using the wavenumber-domain filter as described above. (c) The scattered field (v^{sc}), obtained after subtracting the incident field from the total field.

we can regard the incident wave locally as a smooth plane wave, we have used a wavenumber–frequency domain filter in this example. It is well known that, for each frequency, a double spatial Fourier transform maps a plane wave to a point in the wavenumber space (e.g. Yilmaz 2001), while the scattered energy is mapped over all the wavenumber space. Thus, we first estimate v^{inc} using the wavenumber–frequency domain filter. To this end, we have designed a three-dimensional filter, similar to the single-pass $k_x - k_y - f$ filter discussed by Rowbotham and Goulty (1994). By passing the plane-wave event in the $k_x - k_y - f$ domain and transforming back to the space–time domain, we obtain an

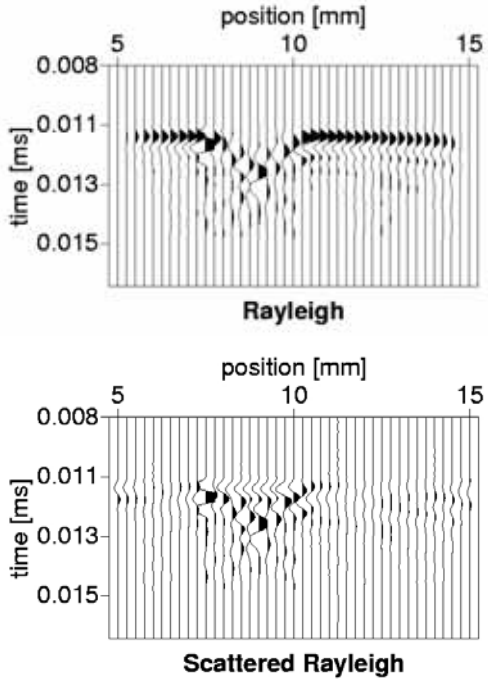

FIGURE 6
(a) Part of the direct Rayleigh wave (event v in the text). This event is used to derive the scattered energy v^{sc}. (b) Seperated scattered energy v^{sc} using a wavenumber-frequency domain filter.

estimate of the incident wave. Finally, we subtract this incident wavefield from the total wavefield as follows:

$$v^{sc}(\mathbf{x},t) = v(\mathbf{x},t) - \beta v^{inc}(\mathbf{x},t)\,, \tag{6}$$

where β is a factor included to account for amplitude differences due to windowing during the filter operation. This factor should be chosen such that the incident wavefield is optimally removed from the entire event, as is shown in Figs 5(a) – (c), that illustrate wavefield separation in the space–time domain. In Fig. 5(a), a time slice of the total field is shown, while in Fig. 5(b), we show the estimated incident field using the procedure described above. Since we used a very narrow filter in the wavenumber domain, we can still observe some edge effects in this display. In Fig. 5(c), the difference between the total field and the estimated incident field is shown. In this example, $\beta = 1.12$ gave the best result. Inspection of Figs 5(a) and 5(c) confirms that we have removed most of the coherent event and left the scattered energy, as shown in Fig. 5(c).

Imaging

Figure 6(a) shows the direct Rayleigh wave in the cross-line direction above the cavity. The scattering can be clearly observed between 7 and 11 mm. The scattered energy, i.e. the energy after wavefield separation, is shown in Fig. 6(b). The next step is to estimate the impedance function with our inversion algorithm. Using

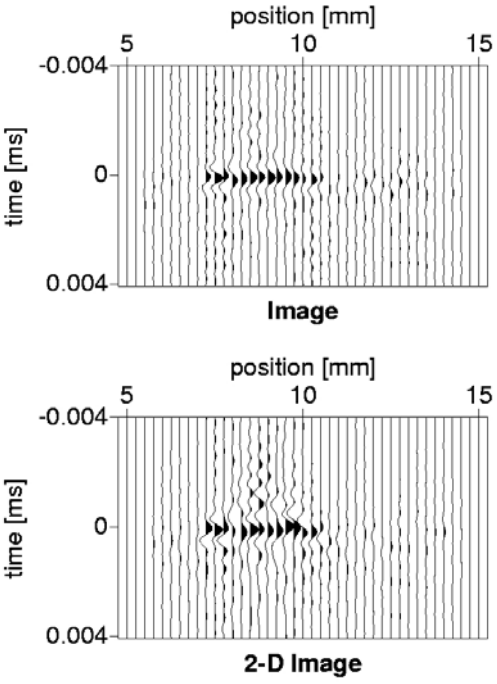

FIGURE 7
(a) Image of the cavity along the same line as in Fig. 6. (b) Image of the same line, now obtained with 2D inversion.

an estimate of the Rayleigh-wave velocity in aluminum (from the data, we estimate $c_R \approx 3000$ m/s), we obtain the impedance function shown in Fig. 7(a). We observe that the energy has been focused in the correct position of the cavity at time $t = 0$. Compared to the scattered field shown in Fig. 6(b), the spatial resolution has been improved, which makes the image useful for accurately localizing near-surface objects. We also observe that the image is more localized in time than in the original scattered data. Figure 8 shows a cross-section of the image at $t = 0$, at the surface of the model. The shaded circular shape, slightly left and down from the centre, represents the actual shape and location of the cavity, while the shaded dots in the upper and lower right-hand corners are focused energy due to scattering from surface irregularities that are smaller than the cavity.

So far, we have described a 3D model and imaging scheme; however, without major modifications we can use 2D inversion to obtain similar results. To show this, we selected one data line from the entire volume (the same one that is used in the examples above). This time we constrain the image to be a line-impedance function instead of a surface-impedance function, but we still use a 3D Green's function in our algorithm. Comparing Figs 7(a) and 7(b), we see that 2D inversion gives comparable results to 3D inversion.

SYNTHETIC TEST

In principle, scattered surface waves can be directly observed on a seismic record (e.g. Leparoux *et al*. 2000). The location of the scatterer can then be inferred from the top of the apex of the diffraction, or from where the coherence of the arrivals breaks down (as in Fig. 4, for example). Moreover, data recorded suffi-

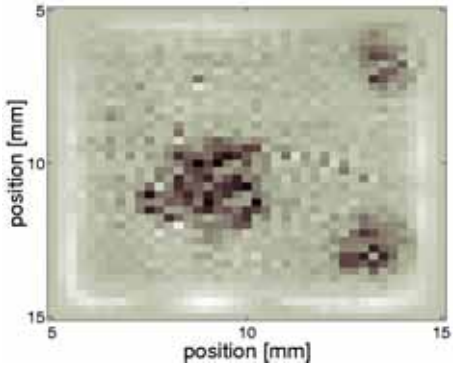

FIGURE 8
Cross-section of the image at $t = 0$ for the first experiment, showing the correct position and size of the cavity. The two darker dots in the upper and lower right-hand corners are due to scattering from surface disturbances that are smaller than the cavity.

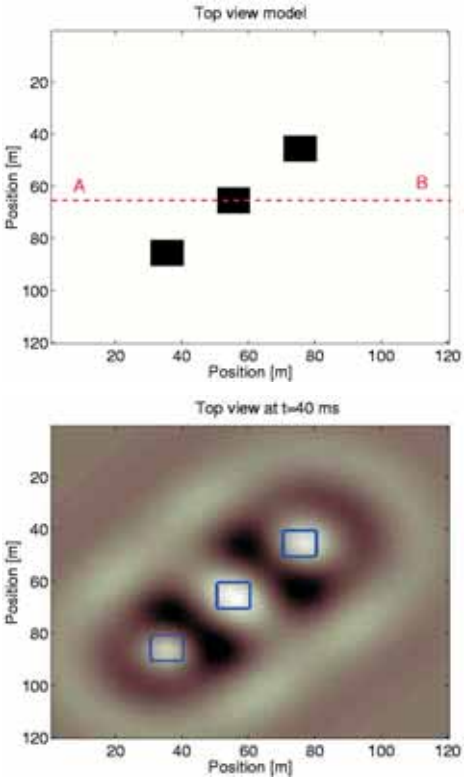

FIGURE 9
(a) Actual model used to generate the data for the first example. (b) Top view of the wave field at 40 ms. Contours indicate the actual locations of the scatterers. Here, we can identify the three scatterers because the peaks in the amplitude of the scattered energy are at the location of the scatterers.

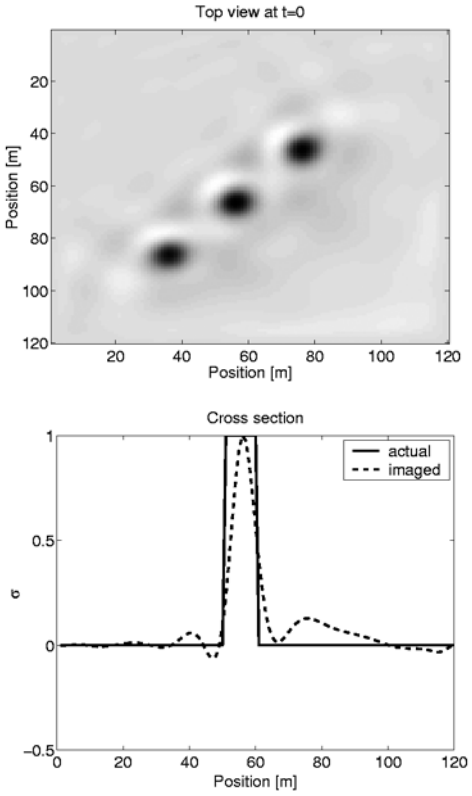

FIGURE 10

(a) Spatial image of the scatters obtained with our imaging algorithm. Clearly, the energy has been focused at the location of the scatterers. (b) Cross-section through the model on the line indicated in (a). The image and the actual scatterer distribution have been normalized to their maximum values.

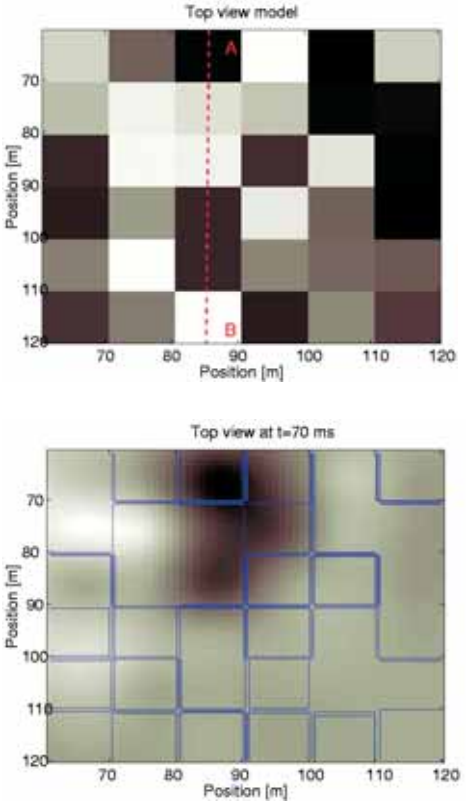

FIGURE 11

(a) Actual model used to generate the data for the second example. (b) Top view of the wave field at 70 ms. Contours indicate the actual locations of the scatterers. Here, individual scatterers cannot be identified because of interference of secondary waves.

ciently densely on an areal grid, allow time-resolved visualization, by watching the wavefield as a function of time (e.g. Scales and Malcolm 2003). In this way, the scatterer can be identified as a secondary source from which scattered waves originate, as in Fig. 3. However, such visual interpretation is only possible if only one, or a few sufficiently spaced scatterers, are located under the receiver array. If two or more scatterers are in the close vicinity of one another, secondary waves interfere and direct identification of diffractions on a shot record may no longer be practical (Herman and Perkins 2004). In these cases, imaging increases the lateral resolution such that individual scatterers can be located. To test whether our algorithm can resolve different scatterers, we have applied it to synthetic data from models with more than one scatterer. We use a 3D elastic modelling code (Riyanti and Herman 2004) to generate the synthetic data.

Model

The vertical velocity was calculated at 1 m intervals at the surface of a 120×120 m^2 area. The source is excited at position $x = 0$, $y = 0$ m at the surface of the model, with a dominant wavelength of about 20 Hz. The S-wave velocity of the embedding medium is 1000 m/s and its density is $\rho^0 = 1500$ kg/m^3. The Rayleigh wavelength is about 40 m. In the first test, three scatterers are located 5 m below the surface. The area of the scatterers is 10×10 m^2, while the vertical extent is 20 m and the densities range from 3500 to 4000 kg/m^3. A top view of this 120×120 m^2 model is shown in Fig. 9(a). In the second model with the same embedding and source position as the first one, 36 scatterers of volume 10×10×10 m^3 are placed in a 60×60 m^2 domain, 5 m below the surface. The densities of these scatterers are chosen from a random normal distribution in the interval 500–4000 kg/m^3. A top view of the scattering domain is shown in Fig. 11(a). Note that this domain occupies the 60×60 m^2 area in the fourth quadrant on the lower right of the model shown in Fig. 9(a).

Results

In Fig. 9(b), we show a constant-time plot of the wavefield at $t = 40$ ms. The scatterers are located far enough apart to be distinguished by looking for the amplitude peaks in the constant-time plot. The contours indicate the actual locations of the scatterers. The image obtained with our method is shown in Fig. 10(a). The scatterers are imaged at the correct locations. Compared to Fig. 9(b), the

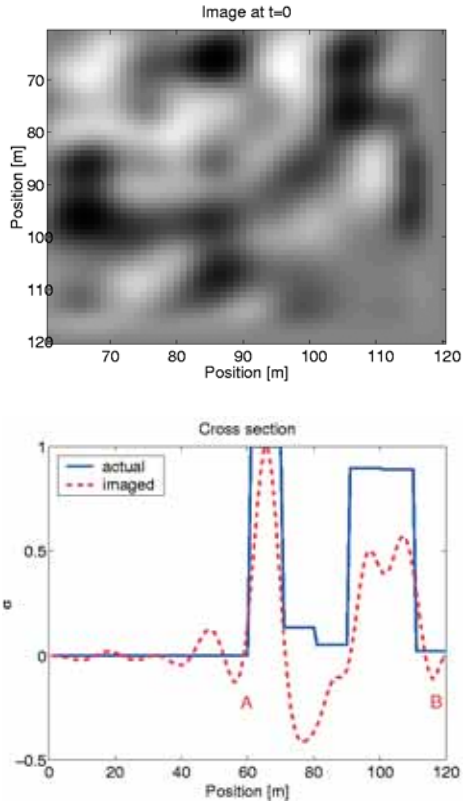

FIGURE 12
(a) Spatial image of the scatterers obtained with our imaging algorithm. The energy has been focused at the location of the scatterers (compare with Fig. 11a). (b) Cross-section through the model on the line indicated in Fig. 11(a). The image and the actual scatterer distribution have been normalized to their maximum values.

spatial resolution has been increased. In Fig. 10(b), we show a cross-section through the image, together with the corresponding cross-section from the actual model. Both have been scaled to their maximum values. This is necessary because we do not obtain an actual value of the contrast but a value that is proportional to the contrast (see equation (3)). However, for accurately locating the scatterer, this is not a limitation. This test shows that we can resolve more than one scatterer. Next, we image data from the model shown in Fig. 11(a). A constant-time plot at t = 70 ms (Fig. 11b) shows that the strongest amplitudes can no longer be associated with the scatterer locations as indicated by the contours. Because of the interference of the scattered surface waves, these amplitude peaks shift location in time, so that even with time-resolved data analysis, the scatterer locations cannot be resolved. In the image (Fig. 12a), scatterers have been resolved and we can identify individual scatterers when compared to Fig. 11(a). Moreover, the (relative) strengths of the contrasts are fairly well estimated. This is shown in Fig. 12(b), where we compare a scaled cross-line from the model and from the image. However, the relative strength of the image is not estimated entirely correctly along this line, which we would expect because the impedance function is proportional to the actual contrast (see equation (3)). This is because the spacing between scatterers is about one-quarter of the Rayleigh wavelength, making it difficult to resolve the interference completely (i.e. this is beyond the resolution that can be obtained using the Rayleigh wave).

DISCUSSION AND CONCLUSIONS

Near-surface heterogeneities cause ground roll to generate scattered surface waves. We have shown that it is possible to obtain spatial images of these near-surface heterogeneities from these scattered surface waves. Our first example showed that this method can be used to process data from multichannel surface-wave records. In the second part of this paper, we have shown that by using the imaging algorithm, we can identify individual scatterers, when interference makes it impossible to resolve them in the shot record. Moreover, we can estimate their relative strengths fairly well when compared to the actual contrasts. By keeping the image at a constant depth, but allowing it to depend on frequency, we convert the depth dependence into frequency dependence (as in a dispersion relation). So far, it is unclear how any information about the depth or vertical size of the heterogeneities is contained in the image, but in the future we plan to study this issue both qualitatively and quantitatively. In addition, we intend to pursue a more rigorous analysis of the inversion process; thus far, our results lack a data error analysis and, therefore, confidence levels on the final results. However, we expect that this method can be useful for imaging the shallow subsurface. Applications may be found in geotechnical engineering, where underground cavities or faults have to be located, or even in environmental engineering, where the problem may be to identify aquifers or detect land-mines.

ACKNOWLEDGEMENTS

Part of the work presented in this paper was carried out while X.C. was a visitor in the Physical Acoustics Laboratory (PAL) at Colorado School of Mines. He would like to thank everyone at PAL and the Center for Wave Phenomena for their hospitality and many fruitful discussions. The work of X.C. and C.D.R. was supported by the Dutch Technology Foundation (STW). This work was partially supported by the National Science Foundation (EAR-0337379) and the Army Research Office (DAAD19-03-1-0292).

REFERENCES

Aki K. and Richards P.G. 1980. *Quantitative Seismology*: *Theory and Practice*. W.H. Freeman & Co.

Behoodian A., Scott Jr. W.R. and McClellan J.H. 1999. Signal processing of elastic surface waves for localizing land mines. 33rd Asilomar Conference on Signals, Systems and Computers, Asilomar, Ca.

Blonk B., Herman G.C. and Drijkoningen G.G. 1995. An elastodynamic inverse scattering method for removing scattered surface waves from field data. *Geophysics* **60**, 1897–1905.

Campman X.H., van Wijk K., Scales J.A. and Herman G.C. 2004. Imaging and suppressing near-receiver scattered waves. *Geophysics*, in print.

Hansen P.C. 1997. *Rank-deficient and Discrete Ill-posed Problems: Numerical Aspects of Linear Inversion*. SIAM.

Harr M.E. 1966. *Foundations of Theoretical Soil Mechanics*. McGraw–Hill Book Co.

Herman G.C. and Perkins C. 2004. Predictive scattered noise removal. 66th EAGE Conference, Paris, France, Extended Abstracts, D027.

Herman G.C., Milligan P.A., Huggins R.J. and Rector J.W. 2000. Imaging shallow objects and heterogeneities with scattered surface waves. *Geophysics* **65**, 247–252.

Leparoux D., Bitri A. and Grandjean G. 2000. Underground cavity detection: a new method based on seismic Rayleigh waves. *European Journal of Environmental and Engineering Geophysics* **5**, 33–53.

Los H.S., Herman G.C. and Hölscher P. 2001. Dynamic interaction between train wheels and the subsurface. *Journal of Sound and Vibration* **247**, 917–926.

Mars J., Rector J.W. and Lazaratos S.K. 1999. Filter formulation and wavefield separation of cross-well seismic data. *Geophysical Prospecting* **47**, 610–636.

Nishizawa O., Sato T., Lei X. and Kuwahara Y. 1997. Laboratory studies of seismic wave propagation in inhomogeneous media using a laser Doppler vibrometer. *Bulletin of the Seismological Society of America* **87**, 809–823.

Nolet G. 1977. The upper mantle under Western Europe inferred from the dispersion of Rayleigh modes. *Journal of Geophysics* **43**, 265–286.

Park C.B., Miller R.D. and Xia J. 1998. Ground roll as a tool to image near-surface anomaly. 68th SEG Meeting, New Orleans, USA, Expanded Abstracts, 874–877.

Park C.B., Miller R.D. and Xia J. 1999. Multichannel analysis of surface waves. *Geophysics* **64**, 800–808.

Riyanti C.D. and Herman G.C. 2004. Elastic modeling of near-surface scattering. 66th EAGE Conference, Paris, France, Extended Abstracts, P-094.

Rowbotham P.S. and Goulty N.R. 1994. Wavefield separation by 3D filtering in cross-hole seismic reflection processing. *Geophysics* **59**, 1065–1071.

Scales J.A. and Malcolm A. 2003. Laser characterization of ultrasonic wave propagation in random media. *Physics Review E* **67**, 046618–046624.

Scales J.A. and van Wijk K. 1999. Multiple scattering attenuation and anisotropy of ultrasonic surface waves. *Applied Physics Letters* **74**, 3899–3901.

Snieder R.K. 1987. Surface wave holography. In: *Seismic Tomography* (ed. G. Nolet), pp. 323–337. D. Reidel Pub. Co.

Stokoe II K., Wright G.W., Bay J.A. and Roesset J.M. 1994. Characterization of geotechnical sites by SASW method. In: *Geophysical Characterization of Sites* (ed. R.D. Woods). Oxford Publishers.

Tarantola A. 1984. Linearized inversion of seismic reflection data. *Geophysical Prospecting* **32**, 998–1015.

Westergaard H.M. 1938. A problem of elasticity suggested by a problem in soil mechanics: Soft material reinforced by numerous strong horizontal sheets. Contributions to *The Mechanics of Solids*, dedicated to S. Timoshenko on the occasion of his 60th birthday anniversary. The Macmillan Press.

Yilmaz O. 2001. *Seismic Data Analysis*. Society of Exploration Geophysicists.